Applied Surface Science 481 (2019) 1335–1343

Contents lists available at ScienceDirect

Applied Surface Science

journal homepage: www.elsevier.com/locate/apsusc

Full length article

Effective photocatalytic salicylic acid removal under visible light irradiation using Ag_2S/AgI-Bi_2S_3/BiOI with *Z*-scheme heterojunctions

Xi Chen[a,b], Wenwen Zhang[b], Lixiang Zhang[c,b], Luping Feng[a,b], Jiangwei Wen[b], Jianjing Yang[b], Chunxian Zhang[b], Jie Jiang[d], Hua Wang[a,b,d,*]

[a] School of Chemistry and Chemical Engineering, Harbin Institute of Technology, Harbin, Heilongjiang 150090, PR China
[b] Institute of Medicine and Materials Applied Technologies, College of Chemistry and Chemical Engineering, Qufu Normal University, Qufu, Shandong 273165, PR China
[c] School of Environment, Harbin Institute of Technology, Harbin, Heilongjiang 150090, PR China
[d] School of Marine Science and Technology, Harbin Institute of Technology at Weihai, Weihai, Shandong 264209, PR China

ARTICLE INFO

Keywords:
2D nanosheets photocatalyst
Z-scheme heterojunction
Visible light response
Salicylic acid removal
Hydrogen peroxide production

ABSTRACT

A photocatalyst of Ag_2S/AgI-Bi_2S_3/BiOI was synthesized with *Z*-scheme heterojunctions simply by the S^{2-}-I^- anion exchange route showing broad visible light response and enhanced photogenerated carriers properties. The yielded Ag_2S/AgI-Bi_2S_3/BiOI could feature the reactive active sites of Bi_2S_3/BiOI and Ag_2S/AgI heterojunctions, serving as the photogenerated electron donors and photogenerated electron acceptors, respectively. Ag bridges were generated to ensure the construction of *Z*-scheme strategy, which further improved the migration direction of charge carriers in nanocomposites. Moreover, the analysis of photoluminescence spectra and electrochemical impedance spectroscopy could testified the functions of heterojunctions, which dramatically achieved the enhanced separation and transferring capacity of photogenerated electron-hole pairs in photocatalyst, respectively. In addition, Ag_2S/AgI-Bi_2S_3/BiOI with large specific surface area facilitated the efficient photocatalytic removal of salicylic acid (SA) (up to 89.2%) under visible light. Favorable photocatalytic production of hydrogen peroxide (H_2O_2) were obtained in pure water driven by the visible light. Besides, by the results of capture experiments, DMPO spin trapping ESR spectra and band structures analysis, the *Z*-scheme manner of the nanocomposites could promote the reduction ability of photo-generated electrons so as to produce numerous $\cdot O_2^-$ during the photocatalytic reactions toward the photocatalytic SA removal and H_2O_2 production.

1. Introduction

Salicylic acid (SA) has been widely applied as the momentous raw material in the dyestuff industries and especially the pharmaceutical industries for the preparation of creams, skin-care ointments, and analgesics. As a result, SA can be an environmental pollutant in wastewater that seriously impairs human health [1,2]. Up to date, many methods have been proposed for controlling the water pollution, such as the membrane filtration, activated carbon adsorption, and microbial decomposition [3,4]. In recent years, the development of photocatalysis strategies for wastewater treatments has concentrated many efforts acting as a potentially prospective route to counter the multifarious environmental predicaments [5,6]. Particularly, the semiconductor photocatalysts most known as TiO_2 and ZnO have dominated the commercial status for the long-term basis. Yet, their practical applications have still confronted plenty of limitations like the UV-excited imperfections [7,8]. Therefore, exploring alternative photocatalytic materials especially those with more efficient utilization of solar is a critical task and practically urgent need.

In recent years, there has emerged a novel bismuth oxyiodide (BiOI) photocatalyst with the anisotropic layered crystal structure of $[Bi_2O_2]^{2+}$ interleaved by slabs comprising iodine atoms, displaying some fascinating electric and optical characteristics [9,10]. More interestingly, BiOI enjoys a narrow energy band gap of ~1.8 eV, which exhibits a strong absorption in visible light range, but usually displays a faster recombination rate of photogenerated electron-hole pairs [11]. Not only that, BiOI with 2D nanosheets structure has an advantage for carriers transport along the growth orientation of crystals. Whereas, mean free path of charge carriers would be prolonged from the inside to the surface of the photocatalysts at the same time. To avoid these defects, the construction of effective heterojunction is preferable by coupling with wider band gap semiconductor to improve the separation

* Corresponding author at: School of Chemistry and Chemical Engineering, Harbin Institute of Technology, Harbin, Heilongjiang 150090, PR China.
E-mail address: huawang@qfnu.edu.cn (H. Wang).
URL: http://wang.qfnu.edu.cn (H. Wang).

https://doi.org/10.1016/j.apsusc.2019.03.214
Received 23 January 2019; Received in revised form 12 March 2019; Accepted 20 March 2019
Available online 21 March 2019
0169-4332/

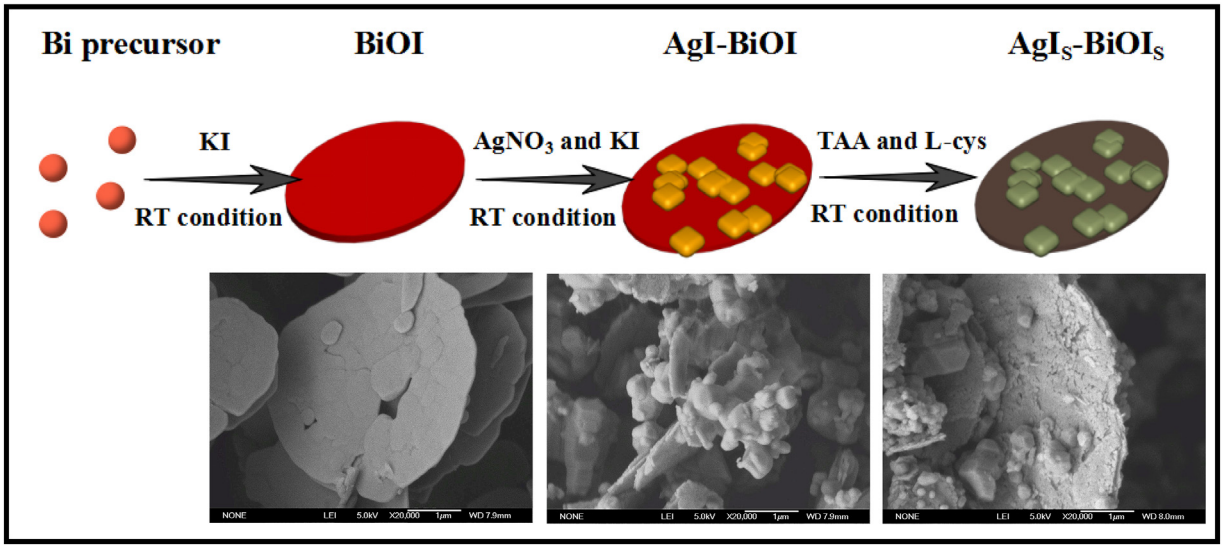

Scheme 1. Schematic illustration of the fabrication procedure of AgI_S-$BiOI_S$ nanocomposite including the nucleation of BiOI nanosheets, growth of AgI nanoparticles on BiOI toward AgI-BiOI, and I^--S^{2-} anion exchanging to transform AgI-BiOI toward AgI_S-$BiOI_S$. These experiments were carried out at room temperature.

efficiency and transport path of photogenerated charge carriers [12,13]. Moreover, silver iodide (AgI) has been commonly utilized as a preeminent photosensitive material in the photographic film industries and environmental pollution treatments. In addition, AgI can exert a strong visible light harvest attributing to its relatively suitable band gap (~2.8 eV) [14–16]. Hence, it has been further employed widely to commendably decorate on other photocatalytic materials, in order to improve both the photocatalytic activity and stability of single material. Ag_2S and Bi_2S_3, as the semiconductors with narrow band gap (Ag_2S ~1.1 eV and Bi_2S_3 ~1.5 eV), are normally employed as the active sites and photosensitizers during photocatalytic reactions for solar-aided wastewater treatments [17,18]. Particularly, abundant types of photocatalysts containing halides have been noticed currently, such as AgI/$Bi_2Sn_2O_7$, MoS_2/BiOI/AgI, Bi@Bi_5O_7I/rGO, AgBr/Ag/$PbBiO_2Br$ [19–22], which can present excellent photocatalytic activities. However, the preparations of composite materials usually accompany complex synthesis methods in most cases. To accommodate the requirements of large-scale production, pursuing more simple synthetic procedure and higher photocatalyst yield seem to be unique, especially for room-temperature synthesis.

Inspired by these pioneering works above, a novel photocatalyst of Ag_2S/AgI-Bi_2S_3/BiOI (denoted as AgI_S-$BiOI_S$) with *Z*-scheme strategy, thereafter, was synthesized simply by the anion exchange route at room temperature. Through coating AgI on BiOI nanosheets, the transfer mode of photogenerated electrons of BiOI could be transformed from 2D to 1D via the construction of Z-scheme heterojunctions. Furthermore, Ag_2S and Bi_2S_3, both as reactive active sites and photosensitizers, were formed on AgI-BiOI nanosheets via the S^{2-}-I^- exchange so as to dramatically aggrandize the light absorption edge of composites. Meantime, AgI could be decomposed to produce Ag^0 to serve as the bridges between Bi_2S_3/BiOI and Ag_2S/AgI for transferring the photogenerated electrons so as to accelerate the separation and transfer of charge carriers. Moreover, the photocatalysis performances of AgI_S-$BiOI_S$ were demonstrated by the photocatalytic SA removal and H_2O_2 production under visible light irradiation. Subsequently, the proposed *Z*-scheme mechanism of AgI_S-$BiOI_S$ for the enhanced photocatalytic activity was discussed.

2. Experiment section

2.1. Materials and instruments

$Bi(NO_3)_3{\cdot}5H_2O$ (99.0%), $AgNO_3$ (99.8%), and L-cysteine (L-cys, 98.5%) were obtained from Sinopharm Chemical Reagent Co. Ltd. (Shanghai, China). C_2H_5NS (TAA, 98.0%) and $Na_2S{\cdot}9H_2O$ (98.0%) were obtained from Aladdin Bio-Chem Technology Co. Ltd. (Shanghai, China). KI (99.0%) was purchased from Damao Chemical Reagent Co. Ltd. (Tianjin, China). Potassium hydrogen phthalate, *p*-hydroxyphenylacetic acid, peroxidase horseradish, salicylic acid and ethanol of analytical grade were used as received. Deionized water (> 18.2 Megohm/cm), which was obtained from an ultra-pure water system (Pall, USA), was used for the preparation of all solutions. XL-300 Xenon Light Source was purchased from Yirida Technology Co. Ltd. (Shenyang, China). Multiscan Spectrum (Infinite M200 PRO) was purchased from Tecan Trading Co. Ltd. (Shanghai, China). Fluorescence spectrophotometer (Fluoromax-4) was purchased from Horiba Jobin Yvon Co. Ltd. (Tianjin, China).

2.2. Synthesis of photocatalytic materials

2.2.1. Synthesis of 2D BiOI

BiOI nanosheets were prepared simply at room temperature. Typically, 0.9701 g of $Bi(NO_3)_3{\cdot}5H_2O$ was hydrolyzed in 15 mL deionized water to acquire the white precursor suspension by ultrasonic dispersed for 20 min. Then, an aliquot of 15 mL aqueous solution contained 0.332 g of KI was slowly dropped to above suspension and stirred for 1 h. Subsequently, the obtained red precipitation was washed with ethanol to eliminate the impurities, and dried at 60 °C overnight.

2.2.2. Synthesis of AgI-BiOI

AgI-BiOI was fabricated through growing AgI nanoparticles in situ onto BiOI nanosheets. Typically, an aliquot of 0.10 g BiOI was dispersed into 10 mL deionized water through ultrasonic treatment. 0.236 g of KI and 0.241 g of $AgNO_3$ were separately dissolved each in 5 mL deionized water. Afterwards, KI solution was added drop by drop into BiOI suspension to be vigorously stirred for 1 h. Then, $AgNO_3$ solution was introduced into the above mixture to be stirred for another 1 h in dark at room temperature. Eventually, the resulting earthy yellow AgI-BiOI products were centrifuged and washed separately with deionized water and ethanol. After being dried at 80 °C for 12 h, they were stored in

dark.

2.2.3. Synthesis of Ag_2S/AgI-Bi_2S_3/BiOI

Ag_2S/AgI-Bi_2S_3/BiOI, defined as AgI_S-$BiOI_S$, was synthesized via anion exchange route using TAA and L-cys at room temperature. The overall fabrication procedure of AgI_S-$BiOI_S$ nanocomposite is schematically illustrated in Scheme 1. In a typical synthesis route, 0.10 g of AgI-BiOI above was dispersed in 20 mL water under constantly vigorous stirring, and further ultrasonically dispersed for 30 min to yield the uniform suspension. After that, a mixture of 2.0 mg TAA and 4.0 mg L-cys in 10 mL water was added into the above suspension to be stirred overnight. Subsequently, the resultant AgI_S-$BiOI_S$ nanocomposites were centrifuged and washed with ethanol, and dried at 60 °C in the end. In addition, the preparations of AgI, Ag_2S, and Bi_2S_3 can be seen in supporting information.

2.3. Characterization of photocatalytic materials

X-ray diffraction patterns of photocatalytic materials were obtained using a diffractometer (XRD, PANalytical/X'pert3) in the range of $2\theta = 20^\circ - 60^\circ$ using Cu Kα radiation. The morphologies involved were examined by using field-emission scanning electron microscopies (SEM, JEOL/JSM-6700F and Carl Zeiss AG/Sigma 500 VP) with energy-disperse X-ray spectroscopy (EDS). TEM and HRTEM images were acquired with transmission electron microscopy (TEM, JEOL/JEM-2100PLUS) with electron energy of 15 kV. Moreover, UV–vis diffuse reflectance spectra of samples were measured using a spectrophotometer (DRS, Shimadzu/UV-3600) with $BaSO_4$ as a reference material. The photoluminescence spectra of samples were characterized using a fluorescence spectrophotometer (PL, Horiba/Fluoromax-4) with an excitation wavelength. Electrochemical impedance spectra (EIS) were obtained using an electrochemical workstation (EIS, CHI760D) with a standard three-electrode system. The reference and counter electrodes were saturated calome and platinum plate, respectively. In addition, 0.10 M KCl aqueous solution was used as the electrolyte.

2.4. Photocatalysis tests

2.4.1. Photocatalytic salicylic acid removal experiments

The photocatalytic testing apparatus was applied composing of glass reactor and light source similar to the previous report [23]. The visible light source was a 300 W Xe-lamp (used 420 nm cut-off filter), with a distance of 20 cm apart from the reaction solution. The average intensity of irradiation was determined to be 4.3 mW·cm^{-2}. Typically, an aliquot of 15 mg photocatalyst was added into 10 mL SA (10 mg/L). Before the illumination, the reaction solutions were stirred for 30 min in darkness at 15 ± 2 °C, so as to reach the adsorption-desorption equilibrium. Then, at the given time intervals, 400 μL reactant suspension was centrifuged to remove the photocatalyst particles, followed by the measurements of absorbance values of SA at λ_{max} = 296 nm by using the Multiscan Spectrum (Tecan/Infinite M200 PRO). Besides, in the capture experiments for probing the active reactive species, the radical scavengers (1.0 mM), including hydroxyl radicals scavenger (isopropanol, IPA), holes scavenger (ethylenediaminetetraacetic acid, EDTA-2Na), and superoxide radicals scavenger (benzoquinone, BQ), were separately injected into the reaction system to be tested according to the same procedure.

2.4.2. Photocatalytic hydrogen peroxide production experiments

Typically, an aliquot of 20 mg photocatalyst was added into 10 mL water. The reaction solutions were stirred for 1 h in darkness at 15 ± 2 °C before the illumination, so as to achieve the adsorption-desorption equilibrium among dissolved oxygen, water, and photocatalysts. An aliquot of 500 μL reactant suspension was centrifuged to remove the photocatalyst particles at the given time intervals, and then 300 μL of obtained clear solution was preserved rapidly. Afterwards, a certain volume of different fluorescent reagents of potassium hydrogen phthalate (8.2 g/L), *p*-hydroxyphenylacetic acid (270 mg/L), and peroxidase horseradish (30 mg/L) were successively introduced into the reaction system. After standing for 2 h, 1.0 mL NaOH (1.0 M) was added into 1.0 mL of solution above to be further mixed for 10 min. The concentrations of hydrogen peroxide were measured by using the POHPAA analysis method [24,25], in which the fluorescent measurements were conducted with the excitation wavelength of 315 nm using the fluorescence spectrophotometer (Horiba/Fluoromax-4).

3. Results and discussion

3.1. Lattice strains analysis and phase structure of photocatalytic materials

The photocatalyst of Ag_2S/AgI-Bi_2S_3/BiOI, defined as AgI_S-$BiOI_S$, was prepared by substituting S^{2-} for I^- species to form Ag_2S and Bi_2S_3 nanoparticles on AgI-BiOI. Herein, the lattice strains analysis was initially performed for AgI_S-$BiOI_S$ according to Williamson and Hall equation [26,27]:

$$B\cos\theta/\lambda = \eta \sin\theta/\lambda + D$$

where B is the full width at half-maximum of the X-ray diffraction peak, θ represents the Bragg diffraction angle, λ represents the X-ray wavelength, η represents lattice strain, D is the Intercept. A curve that plots $B\cos\theta/\lambda$ on the y axis and $\sin\theta/\lambda$ on the x axis is drawn, and the slope of the curve represents the strain of the sample. As is well-known, the discrepancy of the lattice constant accounts for the stress emerging from the interface of composites, distorting the crystal lattice structure eventually. The results of lattice stress analysis were shown in Fig. 1. Accordingly, BiOI nanosheets could primarily extend along two dimensional orientations, showing a positive stress for tensile force (+0.46%). On the contrary, the expression of negative strain for compressive force implies that the growth of AgI could compress the lattice facets of BiOI (−0.90%), hence, the force orientations could not

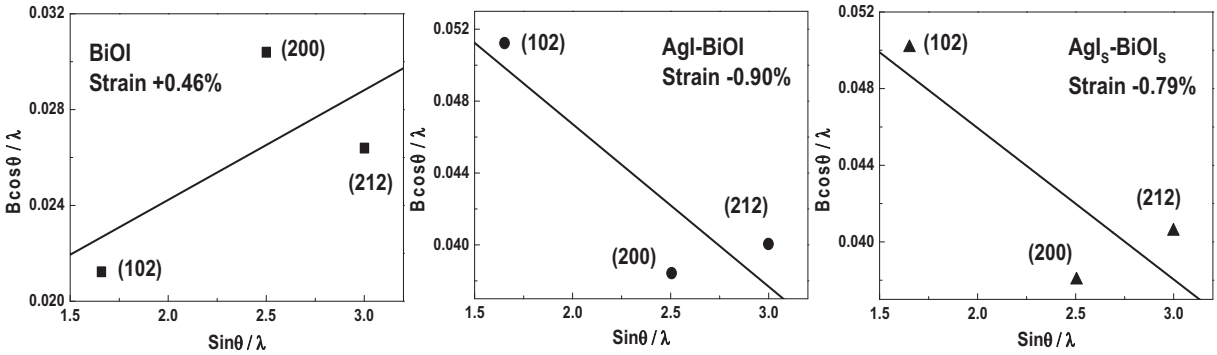

Fig. 1. Williamson-Hall plots of different as-prepared samples.

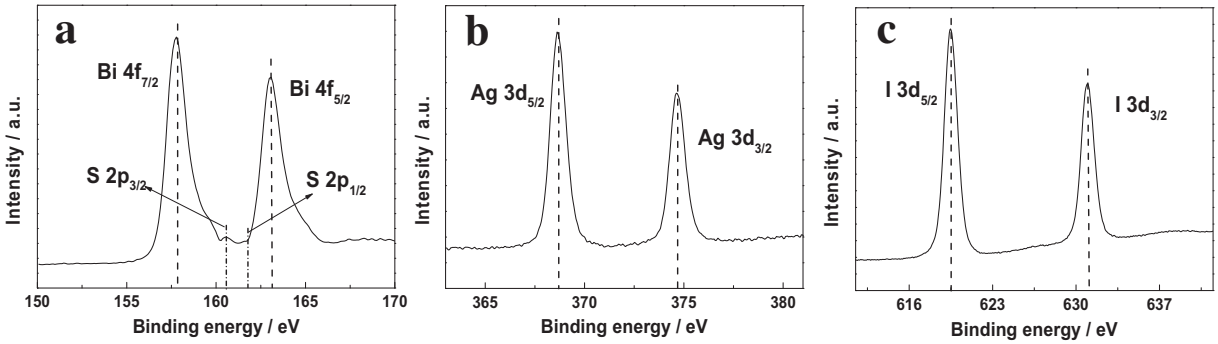

Fig. 2. XPS spectra of Bi 4f and S 2p (a); Ag 3d (b); I 3d (c).

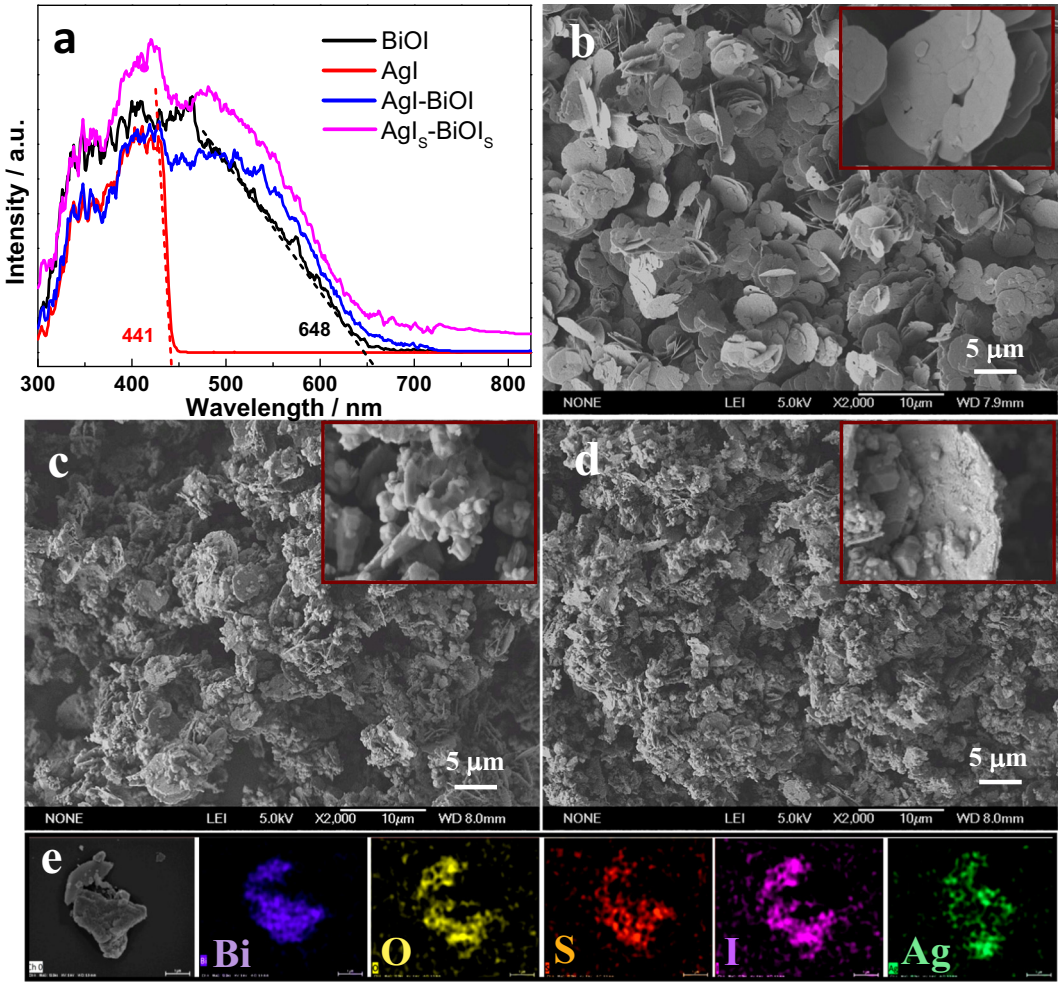

Fig. 3. UV–vis/DRS spectra of different photocatalyst samples (a); SEM images of BiOI (b), AgI-BiOI (c), and AgI_S-$BiOI_S$ (d); EDS element mapping of AgI_S-$BiOI_S$ composing of Bi, O, S, I, and Ag elements (e).

be driven along that of BiOI growth principally. Notably, the lattice strain of the developed AgI_S-$BiOI_S$ (−0.79%) is basically similar to that of AgI-BiOI, indicating that Ag_2S and Bi_2S_3 was deposited on the surface of AgI-BiOI with high dispersion instead of agglomeration. In addition, phase structure analysis was carried out for AgI_S-$BiOI_S$, with the X-ray diffraction patterns shown and discussed in Fig. S1, confirming the successful formation of the photocatalyst.

3.2. Surface element compositions of photocatalytic materials

The chemical states of contributed elements on the surface of AgI_S-$BiOI_S$ were determined by X-ray photoelectron spectroscopy (XPS) with the results shown in Fig. 2. The signal of lattice oxygen is covered by adsorbed oxygen. Two individual peaks situated at 159.4 and 164.1 eV are associated to Bi4$f_{7/2}$ and Bi4$f_{5/2}$, revealing that the chemical state of Bi is trivalent. The signals at 160.7 and 161.9 eV are the characteristic peaks of S^{2-} (Fig. 2a) [18]. The binding energies of 368.1 and 374.1 eV assigned to Ag4$f_{7/2}$ and Ag4$f_{5/2}$ can be proved that Ag is in the state of Ag^+ (Fig. 2b). The binding energies of 619.5 and 631.1 eV observed from Fig. 2c belong to the I^{2-} in nanocomposite [19]. Therefore, the aforementioned data further verify the successful preparation of AgI_S-$BiOI_S$ photocatalyst.

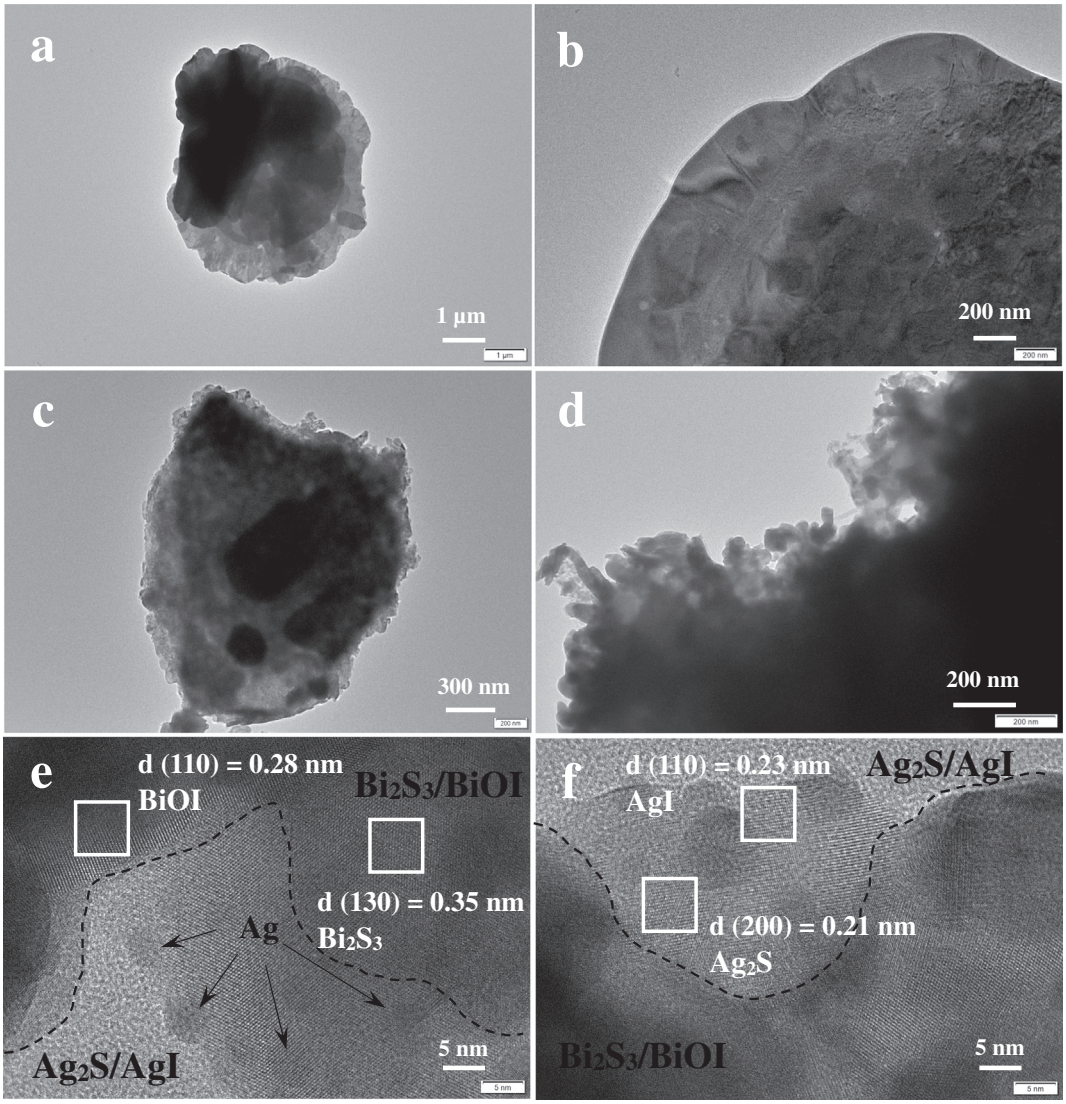

Fig. 4. TEM images of BiOI (a, b) and AgI_S-$BiOI_S$ (c, d) with HRTEM images showing Bi_2S_3/BiOI and Ag_2S/AgI heterojunctions (e, f).

3.3. Optical properties of photocatalytic materials

It is widely recognized that light harvesting ability is one of the key factors for the evaluation of the performances of photocatalysts. For this purpose, the investigation with diffuse reflectance spectra was performed for the as-prepared AgI_S-$BiOI_S$ in comparison with AgI, BiOI, and AgI-BiOI (Fig. 3a). The band gaps of the samples were estimated according to the following formula, with the relevant values shown in Table S1 [28,29]:

$$\lambda g = 1239/Eg$$

where λg is the observed optical absorption edge, Eg represents the band gap. As seen, all of the as-prepared materials can show favorable visible light responses, as is typical of light absorption caused by band transitions from the valence bands to the conduction bands. To be specific, these absorption edges of BiOI (648 nm) and AgI (441 nm) can correspond to the band gaps of 1.9 and 2.8 eV, respectively, suggesting that BiOI can exhibit a broader optical harvest than that of AgI. Not only that, the developed AgI_S-$BiOI_S$ can obtain a dramatically broadened range of visible light absorption over 800 nm. The main reason is thought to involve the generation of Ag_2S and Bi_2S_3 materials in the nanocomposite, which possess smaller band gaps than those of AgI or BiOI as revealed in Fig. S2, so as to widen the optical absorption edge of AgI_S-$BiOI_S$.

3.4. Surface morphologies and microstructures of photocatalytic materials

The morphologies of different photocatalystic samples above were characterized using scanning electron microscopy (SEM), with the results shown in Fig. 3b–d. One can note that BiOI can be composed of massive nanosheets with smooth surface and thin thickness (Fig. 3b). Importantly, this type of 2D structure can not only be in favor of the light penetration and absorption, but also provide a larger specific surface area for exposing more active sites, thus enhancing the contact of photocatalysts with organic pollutants. Moreover, compared to the common bulk AgI materials (Fig. S3), AgI nanoparticles could grow with smaller sizes on the surface of BiOI nanosheets due to the steric hindrance effect between nanosheets (Fig. 3c). Fig. 3d reveals that there is no obvious structure variation after the formation of AgI_S-$BiOI_S$ by the anion exchanging route, but showing the rougher surfaces. Additionally, the elements analysis was conducted for AgI_S-$BiOI_S$ using energy dispersive spectroscopy (EDS), with the results shown in Fig. 3e. One can see that Bi, O, S, I, and Ag elements could be uniformly distributed throughout the nanocomposite, in good agreement with the results of X-ray diffraction patterns (Fig. S1) and lattice strains analysis above (Fig. 1).

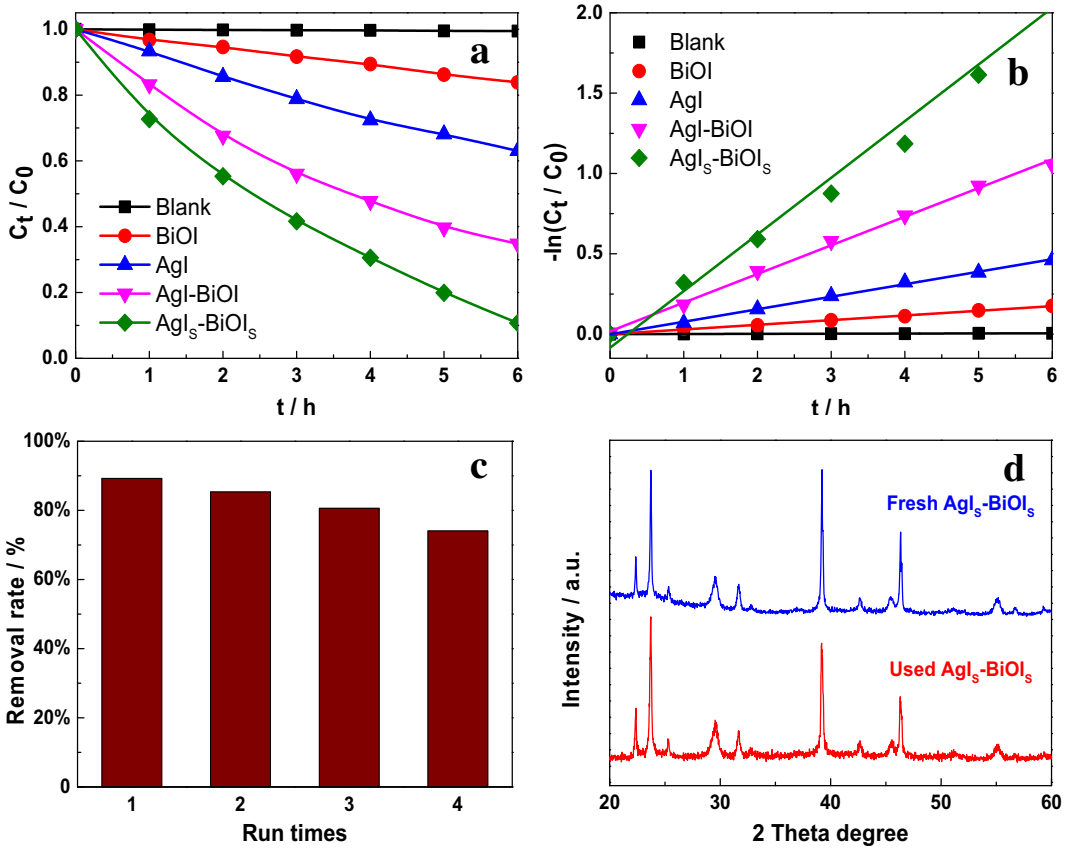

Fig. 5. Photocatalytic removal SA profiles with different synthesized products (a); photocatalytic removal SA kinetics with different samples (b); recycling use results of AgI_S-$BiOI_S$ for photocatalytic degradation (c); XRD patterns of AgI_S-$BiOI_S$ before and after photocatalytic degradation (d).

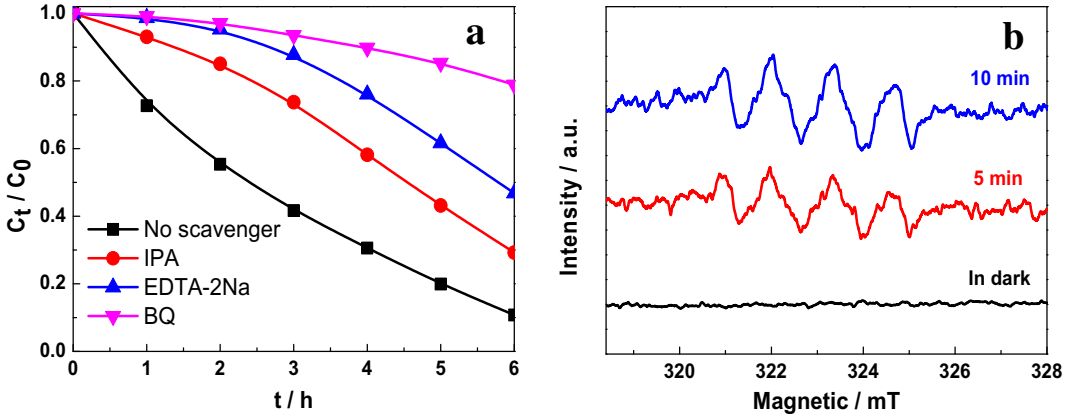

Fig. 6. Reactive species trapping experiments using benzoquinone (BQ), isopropanol (IPA), and ethylenediaminetetraacetic acid (EDTA-2Na) of 1.0 Mm, which were used as the superoxide radicals ($\cdot O_2^-$) scavenger, hydroxyl radicals ($\cdot OH$) scavenger and holes (h^+) scavenger to be injected into the reaction system, respectively (a); DMPO spin trapping ESR spectra of AgI_S-$BiOI_S$ for DMPO-$\cdot O_2^-$ in methanol (b).

Transmission electron microscopy (TEM) was further utilized to evaluate the morphological transformation of AgI_S-$BiOI_S$ during the anion exchanges process (Fig. 4). As expected, BiOI could present the 2D nanosheet structure with smooth surface (Fig. 4a–b). After adding TAA and L-cys, however, AgI-BiOI nanosheets could be turned into heterogeneous Ag_2S/AgI and Bi_2S_3/BiOI nanoparticles with less sizes (Fig. 4c–d), which would improve the specific surface area of AgI_S-$BiOI_S$. Moreover, Fig. 4e–f testify the presences of Bi_2S_3/BiOI and Ag_2S/AgI heterojunctions in the AgI_S-$BiOI_S$. Herein, the lattices, which were measured from the selected areas, illustrate the spacings of 0.28 nm, 0.35 nm, 0.23 nm and 0.21 nm, corresponding to the (110) lattice facet of tetragonal BiOI, the (130) lattice plane of orthorhombic Bi_2S_3, the (110) lattice facet of hexagonal AgI, and the (200) lattice facet of monoclinic Ag_2S, respectively [30–33]. Besides, Ag nanoparticles could additionally grow on the heterogeneous Ag_2S/AgI through the electron beam bombardment or light irradiation, showing an average size of about 5.0 nm in diameter.

3.5. Photocatalytic salicylic acid removal of photocatalytic materials

To assess the photocatalytic performances of the nanosheet photocatalyst of AgI_S-$BiOI_S$, the photocatalytic SA removal tests were carried out under visible light, taking AgI, BiOI, and AgI-BiOI for the comparison, with the results shown in Fig. 5a–c. As can be seen from Fig. 5a,

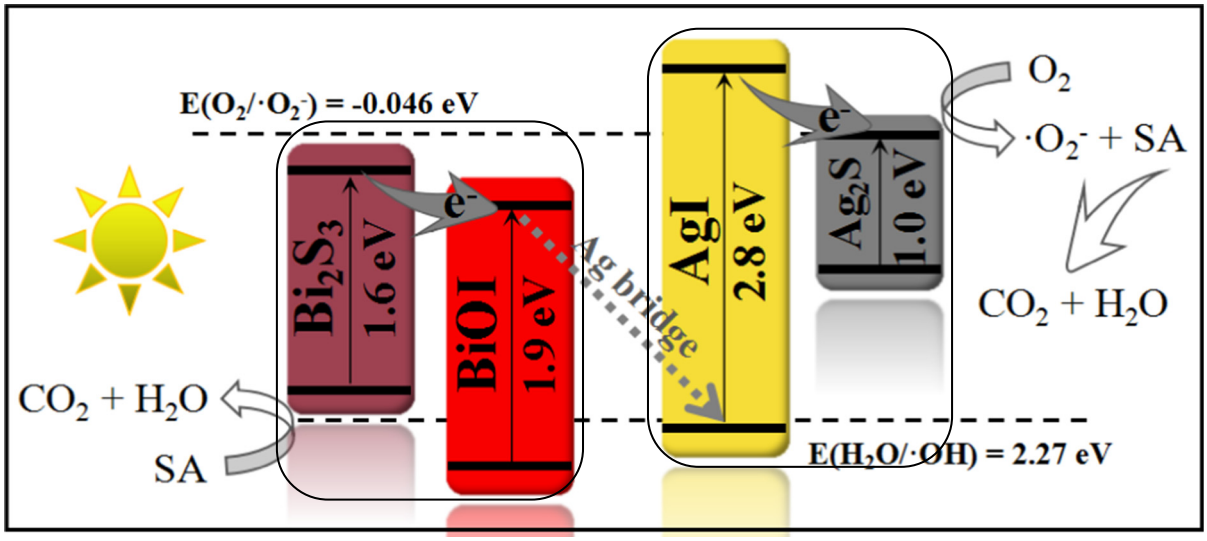

Fig. 7. Possible photocatalytic reaction mechanism of AgI_S-$BiOI_S$ nanocomposite.

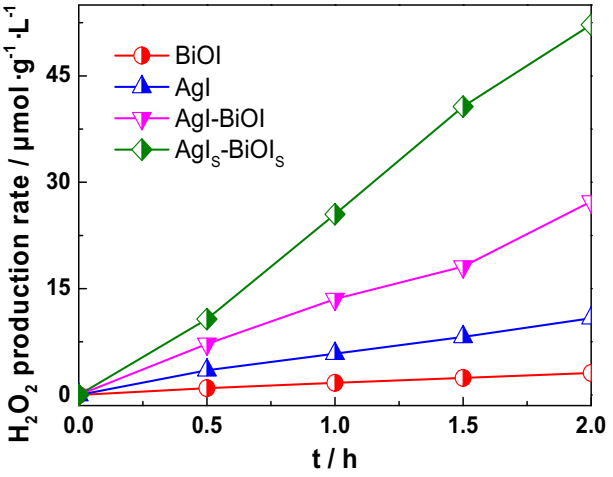

Fig. 8. The profiles of photocatalytic H_2O_2 production with different products.

different photocatalytic products can have various abilities in the photocatalytic SA removals. As expected, the developed AgI_S-$BiOI_S$ can present the highest photocatalytic activity, allowing for 89.2% removal of SA within six-hour irradiation of visible light. Further, the photocatalytic reaction kinetics of SA removal was comparably investigated with the data illustrated in Fig. 5b, where the photo-removal rates were calculated according to the kinetic equation [34,35]:

$$-\ln(C_t/C_0) = kt + b$$

where C_t and C_0 are the concentrations of SA in solution at time t and 0, respectively, k is the rate constant, and b is the intercept. The parameter $-\ln(C_t/C_0)$ is proportional to reaction time t basically, indicating that the SA removal should follow the pseudo-first-order reaction kinetics. Accordingly, the photo-removal rates obtained for BiOI, AgI, AgI-BiOI, and are 0.029, 0.078, 0.178, and 0.353 h^{-1}, respectively. Moreover, the optical stability of AgI_S-$BiOI_S$ was evaluated by repeatedly performing the photocatalytic SA removal experiments (Fig. 5c). One can find that the developed photocatalyst could maintain a pretty high efficiency of SA removal, i.e., 74.0% after being reused for four cycles. Also, the XRD patterns of AgI_S-$BiOI_S$ before and after photocatalytic SA removal were displayed in Fig. 5d. It was found that the nanocomposites could exhibit no significant change in the phase structures, showing a favorable photostability.

In addition, the capture experiments were carried out to ascertain the primary active substances of AgI_S-$BiOI_S$ in photocatalytic SA removal reactions (Fig. 6a) [36,37]. Accordingly, the SA removal reactions could be dramatically restrained by BQ therein, manifesting that the $\cdot O_2^-$ act as the dominant active substances of AgI_S-$BiOI_S$ for the photocatalytic SA removal. Furthermore, electron spin resonance (ESR) characterization was conducted to testify the existence of $\cdot O_2^-$ in the photocatalysis reactions. As illustrated in Fig. 6b, no signals could be detected in the darkness until the AgI_S-$BiOI_S$ was exposed to visible

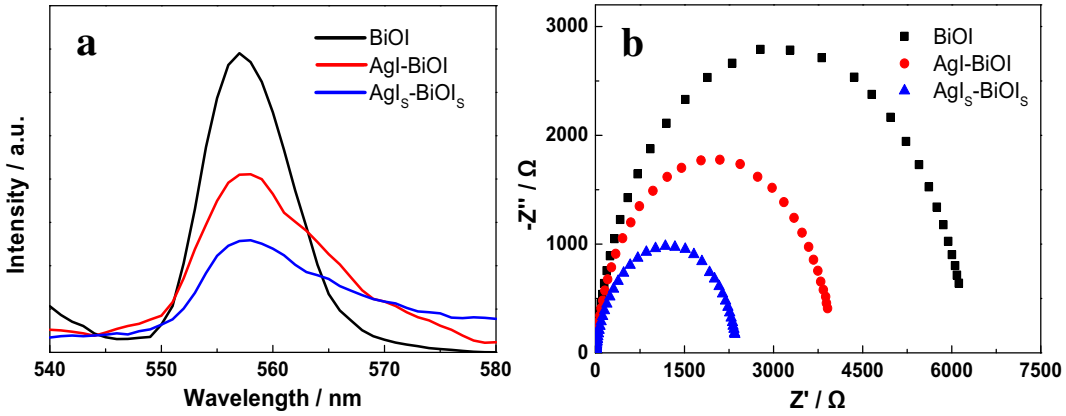

Fig. 9. PL spectra of different products (a); Nyquist plots for EIS of different products (b).

light. It was found that the characteristic peaks of DMPO-$\cdot O_2^-$ could be perceived in methanol, and their intensities increased significantly with the irradiation time went on, indicating that $\cdot O_2^-$ was continually generated during the photocatalytic degradation.

3.6. Possible photocatalytic mechanism of photocatalytic materials

To explored the possible photocatalytic mechanism, the energy band location of AgI_S-$BiOI_S$ was calculated according to the following formulas (Table S1) [38,39]:

$$E_{CB} = X - E_0 - 0.5Eg \quad (1)$$

$$E_{VB} = E_{CB} + Eg \quad (2)$$

where X is the absolute electronegativity of the semiconductor, E_0 represents to the energy of the free electron on the hydrogen scale (4.5 eV). E_{CB} refers the conduction band (CB), E_{VB} is the valence band (VB), and Eg signifies the band gap of the semiconductor. On the basis of the data of capture experiments and energy band structure analysis above, the possible photocatalysis mechanism of AgI_S-$BiOI_S$ was thereby proposed, as schematically illustrated Fig. 7. Herein, since the CB of BiOI presents a more negative potential than the Fermi energy level of Ag, the photogenerated electrons of BiOI transfers to Ag bridges through the schottky barrier [40,41]. Then, so photogenerated electrons of Ag bridges further transfers to the VB of AgI due to the VB of AgI was more positive than that of the Fermi energy level of Ag, leading to a *Z*-scheme transfer pathway. Importantly, the Bi_2S_3 obtained from BiOI through S^{2-}-I^- exchange route can serve as photogenerated electron donors. Also, the Ag_2S gained from AgI can act as photogenerated electron acceptors. Subsequently, SA was degraded by the powerful free radicals produced by the redox reaction of photogenerated carriers on Bi_2S_3 and Ag_2S of AgI_S-$BiOI_S$.

Retrospectively, such a type of transfer pathway of AgI_S-$BiOI_S$ could also be testified from the trapping experiments of reactive species and DMPO spin trapping ESR spectra above (Fig. 6a–b). It was discovered that the conduction band potential of BiOI was more positive than that of $E_0(O_2/O_2^-)$ [16], thus the photogenerated electrons on BiOI cannot restore O_2 to $\cdot O_2^-$. On the contrary, the photogenerated electrons on Ag_2S with the strong reduction power can transform O_2 into $\cdot O_2^-$, owing to the their more negative potential. Therefore, $\cdot O_2^-$ serve as main active substances suggesting the successful formation of *Z*-scheme strategy in AgI_S-$BiOI_S$. Notably, compared to the traditional heterojunctions, the so constructed Z-scheme heterojunctions of photocatalyst can feature the elevating the reduction potential of photogenerated electrons rather than the declining ones.

3.7. Hydrogen peroxide production of photocatalytic materials

Besides, it is well known that H_2O_2 is a potent oxidant, which can directly oxidize various refractory organic pollutants. Generally, H_2O_2 can be generated through the two-step single-electron transfer routes ($O_2 \rightarrow \cdot O_2^- \rightarrow H_2O_2$) [42]. In the current work, AgI_S-$BiOI_S$ could feature a Z-scheme system for generating a great deal of $\cdot O_2^-$. Accordingly, AgI_S-$BiOI_S$ was further applied for the H_2O_2 production under visible light (Fig. 8). As seen, single BiOI can hardly exhibit H_2O_2 generation owing to its more positive potential of CB (+0.76 eV), so that the excited photogenerated electrons from CB could not restore O_2 to $\cdot O_2^-$. In contrast, AgI_S-$BiOI_S$ with Z-scheme heterojunctions could display the highest H_2O_2 production rate than that of other photocatalysts in pure water. These results imply that the improved reducing capacity of photogenerated electrons could play a key role in the effective photocatalytic H_2O_2 generation.

3.8. Modified photogenerated carriers of photocatalytic materials

In order to get further insights into the influence of the heterostructures on the photogenerated charge carriers in AgI_S-$BiOI_S$, photoluminescence (PL) spectra analysis [43] and electrochemical impedance spectroscopy (EIS) measurements [44] were carried out by comparing with BiOI and AgI-BiOI photocatalysts (Fig. 9). As seen, AgI_S-$BiOI_S$ can display the highly separation efficiency and interfacial charge transfer of photo-induced carriers, respectively. Specifically, a more rapid transfer capacity of the photogenerated electrons can benefit for shortening the diffusion path for the electrons transferring onto the surface of semiconductor. Accordingly, AgI_S-$BiOI_S$ could significantly improve the transfer speed and the separation efficiency of photogenerated electron-hole pairs, showing the dramatically enhanced photo-reduction capacity of photogenerated electrons to facilitate the highly efficient photocatalytic SA removal and H_2O_2 production under the visible light.

4. Conclusion

To summarize, a nanosheet photocatalyst of Ag_2S/AgI-Bi_2S_3/BiOI (AgI_S-$BiOI_S$) was synthesized initially with *Z*-scheme heterojunctions simply through the S^{2-}-I^- anion exchange route at room temperature. It was discovered that the introduction of Ag_2S and Bi_2S_3 could dramatically aggrandize the light absorption edge of AgI_S-$BiOI_S$ nanophotocatalyst over the visible light area. The so constructed Ag_2S/AgI and Bi_2S_3/BiOI heterojunctions in the photocatalyst could serve as the photogenerated electron acceptors and photogenerated electron donors during the photocatalysis procedure, respectively. Moreover, Ag bridges could be built in AgI_S-$BiOI_S$ to achieve the Z-scheme strategy, so that the transfer pathway of photogenerated electrons could be significantly converted from the traditional “downstairs” into the novel “upstairs”, thus enhancing the photo-reduction ability of the photogenerated electrons. In addition, the $\cdot O_2^-$ photocatalytically yielded could act as the primary active substances in the photocatalytic reaction system. The developed AgI_S-$BiOI_S$ nanocatalyst could not only allow for the photocatalytic SA removal of 89.2% within six-hour visible light irradiation, but also display a favorable photocatalytic H_2O_2 production rate in pure water. Therefore, the proposed photocatalysis system with Z-Scheme strategy should promise a favorable propulsion toward the practical applications for the efficient photocatalystic removal of various kinds of refractory organic pollutants such as organic phosphorus pesticides, surfactant agents, and toxic macromolecular organics. It is forecasted that the developed photocatalysis system should be functionalized as the two-channel photocatalytic system for the SA removal if simultaneously combined with H_2O_2 photocatalytically produced.

Acknowledgements

This work was supported by the National Natural Science Foundation of China (Nos. 21675099), Major Basic Research Program of Natural Science Foundation of Shandong Province, P. R. China (ZR2018ZC0129), and Science and Technology Development Project of Weihai City (2015DXGJZD002), Shandong Province, P. R. China.

Appendix A. Supplementary data

Supplementary data to this article can be found online at https://doi.org/10.1016/j.apsusc.2019.03.214.

References

[1] Y. Duan, Facile preparation of CuO/g-C_3N_4 with enhanced photocatalytic degradation of salicylic acid, Mater. Res. Bull. 105 (2018) 68–74.
[2] W. Guo, X. Liu, P. Huo, X. Gao, D. Wu, Z. Lu, Y. Yan, Hydrothermal synthesis spherical TiO_2 and its photo-degradation property on salicylic acid, Appl. Surf. Sci. 258 (2012) 6891–6896.
[3] B. Garza-Campos, E. Brillas, A. Hernandez-Ramirez, A. E. Ghenymy, J. L. Guzman-Mar, E. J. Ruiz-Ruiz, Salicylic acid degradation by advanced oxidation processes. Coupling of solar photoelectro-fenton and solar heterogeneous photocatalysis, J.

Hazard. Mater. 319 (2016) 34–42.
[4] L. Nie, Q. Zhang, Recent progress in crystalline metal chalcogenides as efficient photocatalysts for organic pollutant degradation, Inorg. Chem. Front. 4 (2017) 1953–1962.
[5] H. Guo, H.Y. Niu, C. Liang, C.G. Niu, D.W. Huang, L. Zhang, N. Tang, Y. Yang, C.Y. Feng, G.M. Zeng, Insight into the energy band alignment of magnetically separable $Ag_2O/ZnFe_2O_4$ p-n heterostructure with rapid charge transfer assisted visible light photocatalysis, J. Catal. 370 (2019) 289–303.
[6] H. Guo, C.G. Niu, D.W. Huang, N. Tang, C. Liang, L. Zhang, X.J. Wen, Y. Yang, W.J. Wang, G.M. Zeng, Integrating the plasmonic effect and p-n heterojunction into a novel $Ag/Ag_2O/PbBiO_2Br$ photocatalyst: broadened light absorption and accelerated charge separation co-mediated highly efficient visible/NIR light photocatalysis, Chem. Eng. J. 360 (2019) 349–363.
[7] L. Yue, R. Cheng, W. Ding, J. Shao, J. Li, J. Lyu, Composited micropores constructed by amorphous TiO_2 and graphene for degrading volatile organic compounds, Appl. Surf. Sci. 471 (2019) 1–7.
[8] M. Ge, C. Cao, J. Huang, S. Li, Z. Chen, K.Q. Zhang, S.S. Al-Deyab, Y. Lai, A review of one-dimensional TiO_2 nanostructured materials for environmental and energy applications, J. Mater. Chem. A 4 (2016) 6772–6801.
[9] A. Zhang, W. Xing, D. Zhang, H. Wang, G. Chen, J. Xiang, A novel low-cost method for Hg^0 removal from flue gas by visible-light-driven BiOX (X = Cl, Br, I) photocatalysts, Catal. Commun. 87 (2016) 57–61.
[10] Z. Guo, S. Zhu, Y. Yong, X. Zhang, X. Dong, J. Du, J. Xie, Q. Wang, Z. Gu, Y. Zhao, Synthesis of BSA-coated $BiOI@Bi_2S_3$ semiconductor heterojunction nanoparticles and their applications for radio/photodynamic/photothermal synergistic therapy of tumor, Adv. Mater. 29 (2017) 1704136.
[11] B. Long, Y. Huang, H. Li, F. Zhao, Z. Rui, Z. Liu, Y. Tong, H. Ji, Carbon dots sensitized BiOI with dominant {001} facets for superior photocatalytic performance, Ind. Eng. Chem. Res. 54 (2015) 12788–12794.
[12] A. Kudo, Y. Miseki, Heterogeneous photocatalyst materials for water splitting, Chem. Soc. Rev. 38 (2009) 253–278.
[13] L. Sun, L. Xiang, X. Zhao, C.-J. Jia, J. Yang, Z. Jin, X. Cheng, W. Fan, Enhanced visible-light photocatalytic activity of BiOI/BiOCl heterojunctions: key role of crystal facet combination, ACS Catal. 5 (2015) 3540–3551.
[14] J. Zeng, M. Li, A. Liu, F. Feng, T. Zeng, W. Duan, M. Li, M. Gong, C.-Y. Wen, Y. Yin, Au/AgI dimeric nanoparticles for highly selective and sensitive colorimetric detection of hydrogen sulfide, Adv. Funct. Mater. 28 (2018) 1800515.
[15] M.U. Khan, H. You, X. Liu, L. Zhang, J. Fang, Designing novel nonsymmetric Ag/AgI nanoplates for superior photocatalytic activity, Small 14 (2018) 1702948.
[16] F. Chen, Q. Yang, F. Yao, S. Wang, J. Sun, H. An, K. Yi, Y. Wang, Y. Zhou, L. Wang, X. Li, D. Wang, G. Zeng, Visible-light photocatalytic degradation of multiple antibiotics by AgI nanoparticle-sensitized Bi_5O_7I microspheres: enhanced interfacial charge transfer based on z-scheme heterojunctions, J. Catal. 352 (2017) 160–170.
[17] T. Kosmala, D. Mosconi, G. Giallongo, G.A. Rizzi, G. Granozzi, Highly efficient $MoS_2/Ag_2S/Ag$ photoelectrocatalyst obtained from a recycled DVD surface, ACS Sustain. Chem. Eng. 6 (2018) 7818–7825.
[18] S. Adhikari, K.D. Heyoung, Synthesis of Bi_2S_3/Bi_2WO_6 hierarchical microstructures for enhanced visible light driven photocatalytic degradation and photoelectrochemical sensing of ofloxacin, Chem. Eng. J. 354 (2018) 692–705.
[19] H. Guo, C.G. Niu, L. Zhang, X.J. Wen, C. Liang, X.G. Zhang, D.L. Guan, N. Tang, G.M. Zeng, Construction of direct Z-scheme $AgI/Bi_2Sn_2O_7$ nanojunction system with enhanced photocatalytic activity: accelerated interfacial charge transfer induced efficient Cr(VI) reduction, tetracycline degradation and Escherichia coli inactivation, ACS Sustain. Chem. Eng. 6 (2018) 8003–8018.
[20] M.J. Islam, D.A. Reddy, N.S. Han, J. Choi, J.K. Song, T.K. Kim, An oxygen-vacancy rich 3d novel hierarchical $MoS_2/BiOI/AgI$ ternary nanocomposite: enhanced photocatalytic activity through photogenerated electron shuttling in a z-scheme manner, Phys. Chem. Chem. Phys. 18 (2016) 24984–24993.
[21] C. Liang, C.G. Niu, L. Zhang, X.J. Wen, S.F. Yang, H. Guo, G.M. Zeng, Construction of 2D heterojunction system with enhanced photocatalytic performance: Plasmonic Bi and reduced graphene oxide co-modified Bi_5O_7I with high-speed charge transfer channels, J. Hazard. Mater. 361 (2019) 245–258.
[22] H. Guo, C.G. Niu, X.J. Wen, L. Zhang, C. Liang, X.G. Zhang, D.L. Guan, N. Tang, G.M. Zeng, Construction of highly efficient and stable ternary $AgBr/Ag/PbBiO_2Br$ Z-scheme photocatalyst under visible light irradiation: performance and mechanism insight, J. Colloid Interface Sci. 513 (2018) 852–865.
[23] X. Chen, L. Li, W. Zhang, Y. Li, Q. Song, L. Dong, Fabricate globular flower-like $CuS/CdIn_2S_4/ZnIn_2S_4$ with high visible light response via microwave-assisted one-step method and its multipathway photoelectron migration properties for hydrogen evolution and pollutant degradation, ACS Sustain. Chem. Eng. 4 (2016) 6680–6688.
[24] A.L. Lazrus, G.L. Kok, S.N. Gitlin, J.A. Lind, S.E. McLaren, Automated fluorimetric method for hydrogen peroxide in atmospheric precipitation, Anal. Chem. 57 (1985) 917–922.
[25] S. Li, G. Dong, R. Haililia, L. Yang, Y. Li, F. Wang, Y. Zen, C. Wang, Effective photocatalytic H_2O_2 production under visible light irradiation at g-C_3N_4 modulated by carbon vacancies, Appl. Catal. B Environ. 190 (2016) 26–35.
[26] X. Chen, L. Li, W. Zhang, Y. Li, Q. Song, J. Zhang, D. Liu, Multi-pathway photoelectron migration in globular flower-like $In_2O_3/AgBr/Bi_2WO_6$ synthesized by microwave-assisted method with enhanced photocatalytic activity, J. Mol. Catal. A Chem. 414 (2016) 27–36.
[27] S. Khanchandani, P.K. Srivastava, S. Kumar, S. Ghosh, A.K. Ganguli, Band gap engineering of ZnO using core/shell morphology with environmentally benign Ag_2S sensitizer for efficient light harvesting and enhanced visible-light photocatalysis, Inorg. Chem. 53 (2014) 8902–8912.
[28] S. Shenawi-Khalil, V. Uvarov, S. Fronton, I. Popov, Y. Sasson, A novel heterojunction BiOBr/bismuth oxyhydrate photocatalyst with highly enhanced visible light photocatalytic properties, J. Phys. Chem. C 116 (2012) 11004–11012.
[29] L. Ye, J. Liu, C. Gong, L. Tian, T. Peng, L. Zan, Two different roles of metallic Ag on Ag/Agx/BiOX (X = Cl, Br) visible light photocatalysts: surface plasmon resonance and z-scheme bridge, ACS Catal. 2 (2012) 1677–1683.
[30] R. Dong, Y. Hu, Y. Wu, W. Gao, B. Ren, Q. Wang, Y. Cai, Visible-light-driven BiOI-based janus micromotor in pure water, J. Am. Chem. Soc. 139 (2017) 1722–1725.
[31] F. Guo, W. Shi, H. Wang, M. Han, W. Guan, H. Huang, Y. Liu, Z. Kang, Study on highly enhanced photocatalytic tetracycline degradation of type $AgI/CuBi_2O_4$ and z-scheme $AgBr/CuBi_2O_4$ heterojunction photocatalysts, J. Hazard. Mater. 349 (2018) 111–118.
[32] L. Zhao, H.H. Wu, C. Yang, Q. Zhang, G. Zhong, Z. Zheng, H. Chen, J. Wang, K. He, B. Wang, T. Zhu, X.C. Zeng, M. Liu, M.S. Wang, Mechanistic origin of the high performance of yolk@shell Bi_2S_3@N-doped carbon nanowire electrodes, ACS Nano 12 (2018) 12597–12611.
[33] J. Feng, Y. Li, Z. Gao, H. Lv, X. Zhang, Y. Dong, P. Wang, D. Fan, Q. Wei, A competitive-type photoelectrochemical immunosensor for aflatoxin B1 detection based on flower-like WO_3 as matrix and Ag_2S-enhanced $BiVO_4$ for signal amplification, Sensors Actuators B Chem. 270 (2018) 104–111.
[34] Z.M. Yang, G.F. Huang, W.Q. Huang, J.M. Wei, X.G. Yan, Y.Y. Liu, C. Jiao, Z. Wan, A. Pan, Novel Ag_3PO_4/CeO_2 composite with high efficiency and stability for photocatalytic applications, J. Mater. Chem. A 2 (2014) 1750–1756.
[35] X. Chen, L. Li, T. Yi, W. Zhang, X. Zhang, L. Wang, Microwave assisted synthesis of sheet-like $Cu/BiVO_4$ and its activities of various photocatalytic conditions, J. Solid State Chem. 229 (2015) 141–149.
[36] Z. Zhu, P. Huo, Z. Lu, Y. Yan, Z. Liu, W. Shi, C. Li, H. Dong, Fabrication of magnetically recoverable photocatalysts using g-C_3N_4 for effective separation of charge carriers through like-z-scheme mechanism with Fe_3O_4 mediator, Chem. Eng. J. 331 (2018) 615–625.
[37] M. Marchelek, E. Grabowska, T. Klimczuk, W. Lisowski, P. Mazierski, A. Zaleska-Medynska, Visible light photocatalysis employing $TiO_2/SrTiO_3$-BiOI composites: surface properties and photoexcitation mechanism, J. Mol. Catal. 452 (2018) 154–166.
[38] T. Yan, J. Tian, W. Guan, Z. Qiao, W. Li, J. You, B. Huang, Ultra-low loading of Ag_3PO_4 on hierarchical In_2S_3 microspheres to improve the photocatalytic performance: the cocatalytic effect of Ag and Ag_3PO_4, Appl. Catal. B Environ. 202 (2017) 84–94.
[39] J. Jiang, X. Zhang, P. Sun, L. Zhang, ZnO/BiOI heterostructures: photoinduced charge-transfer property and enhanced visible-light photocatalytic activity, J. Phys. Chem. C 115 (2011) 20555–20564.
[40] R.L.Z. Hoye, L.C. Lee, R.C. Kurchin, T.N. Huq, K.H.L. Zhang, M. Sponseller, L. Nienhaus, R.E. Brandt, J. Jean, J.A. Polizzotti, A. Kursumovic, M.G. Bawendi, V. Bulovic, V. Stevanovic, T. Buonassisi, J.L. MacManus-Driscoll, Strongly enhanced photovoltaic performance and defect physics of air-stable bismuth oxyiodide (BiOI), Adv. Mater. 29 (2017) 1702176.
[41] C. Chang, L. Zhu, S. Wang, X. Chu, L. Yue, Novel mesoporous graphite carbon nitride/BiOI heterojunction for enhancing photocatalytic performance under visible-light irradiation, ACS Appl. Mater. Interfaces 6 (2014) 5083–5093.
[42] L. Wang, M. Cao, Z. A, L. Zhang, Dramatically enhanced aerobic atrazine degradation with $Fe@Fe_2O_3$ core − shell nanowires by tetrapolyphosphate, Environ. Sci. Technol. 48 (2014) 3354–3362.
[43] M. Li, L. Zhang, X. Fan, M. Wu, M. Wang, R. Cheng, L. Zhang, H. Yao, J. Shi, Core-shell $LaPO_4/g\text{-}C_3N_4$ nanowires for highly active and selective CO_2 reduction, Appl. Catal. B Environ. 201 (2017) 629–635.
[44] Y. He, L. Zhang, B. Teng, M. Fan, New application of z-scheme $Ag_3PO_4/g\text{-}C_3N_4$ composite in converting CO_2 to fuel, Environ. Sci. Technol. 49 (2014) 649–656.